Dynamical regimes reveal drivers of Earth's growing energy imbalance

Clare E. Singer[1*], Or Hadas[2,*], Marius A. Schulz[3], Rowan Orlijan-Rhyne[3], Franziska Glassmeier[3], Frida Bender[4]

[1]University of Colorado Boulder, Boulder, Colorado, USA
[2]Weizmann Institute of Science, Rehovot, Israel
[3]Max Planck Institute for Meteorology, Hamburg, Germany
[4]Stockholm University and Bolin Centre for Climate Research, Stockholm, Sweden

Key Points:

- Although Earth's energy imbalance (EEI) is increasing globally, local trends are heterogeneous and reflect distinct physical processes.
- By separating Earth into dynamical regimes, we identify five regimes that dominate EEI trends and their leading physical drivers.
- Based on this mechanistic understanding, we qualitatively assess that EEI will continue to increase in the next decades.

*These authors contributed equally to the work.

Corresponding author: Clare E. Singer, clare.singer@colorado.edu

Corresponding author: Or Hadas, or.hadas@weizmann.ac.il

Abstract

Earth's energy imbalance (EEI) has increased substantially over the 21st century in the global mean. However, spatial heterogeneity in the trends makes interpretation challenging. We move beyond the global-mean perspective by decomposing EEI trends into dynamical regimes defined using climatological circulation metrics and show that each regime is governed by distinct physical processes. The tropical ascent regime is dominated by clear-sky trends associated with increased CO_2 and water vapor. Stratocumulus cloud regions in the subsidence regime exhibit strong positive shortwave cloud radiative effect (SWCRE) trends. Midlatitude storm track regime shows SWCRE trends associated with poleward shifts of the storm tracks, and aerosol reduction in the clear-sky. The Southern Hemisphere polar cryosphere exhibits strong SW clear-sky trends driven by sea ice loss. Our process-based, regional framework links the observed EEI increase with physical processes, and provides a basis for projecting continued increase in the near future.

Plain Language Summary

Earth's heating rate is determined by the imbalance between incoming solar radiation and outgoing longwave radiation, known as Earth's energy imbalance (EEI). EEI has increased over the 26 year satellite record, but it is unclear what drives this trend. To improve mechanistic understanding, we divide Earth into five climate regimes and identify the physical drivers of increasing EEI in each regime. We find increases in greenhouse gases, changes in cloud properties and distribution, decreases in aerosol, and sea ice loss are the leading drivers of the trends. Together, these regional processes explain the observed increase in EEI and help clarify why it has increased in the past and how it may change in the future.

1 Introduction

Earth's energy imbalance (EEI) measures the difference between incoming energy from the sun and outgoing energy reflected and emitted by Earth. As such, it represents the net rate at which the Earth system is taking up heat, making it our most fundamental metric for changes in climate. A significant increasing trend of 0.46 ± 0.15 W m^{-2} dec^{-1} in EEI has been observed (Figure 1), based on measurements from the Clouds and the Earth's Radiant Energy System (CERES) satellite instruments (Loeb, Johnson, et al., 2021; Loeb et al., 2024; Mauritsen et al., 2025) and supported by in-situ observations of ocean heat content (Hakuba et al., 2024; Von Schuckmann et al., 2023; Minière et al., 2023). The positive trend is driven by a decrease in shortwave reflection, which is only partially compensated for by an increase in outgoing longwave radiation (Figure 3, Loeb et al. (2024)).

Much of our current understanding of EEI and its trend comes from the global-mean perspective (e.g., Mauritsen et al., 2025). This focus is partly motivated by the conceptual framework of energy balance models (Held et al., 2010; Winton et al., 2010), which also underpin the common decomposition of EEI into forcing and feedback components (Raghuraman et al., 2021; Loeb, Johnson, et al., 2021; Hodnebrog et al., 2024; Ceppi et al., 2026). However, growing evidence points to the importance of processes that are not well captured by a global-mean view. In particular, recent studies have highlighted the central role of clouds in driving EEI trends, especially in the shortwave component. Both Loeb, Johnson, et al. (2021) and Park and Soden (2025) attribute a substantial fraction of the increase in shortwave radiative energy to cloud changes, estimating trends of 0.40 ± 0.18 and 0.57 ± 0.15 W m^{-2} dec^{-1}, respectively. Yet, these cloud-driven changes are highly heterogeneous: their spatial patterns exhibit strong regional contrasts, with opposing trends in different regions (Loeb, Johnson, et al. (2021), their Figure 3a; Figure 3d). This heterogeneity suggests that distinct physical processes govern cloud responses across regions. Understanding these mechanisms is therefore critical both to explain why EEI

has increased faster than predicted by comprehensive models (Raghuraman et al., 2021; Hodnebrog et al., 2024; Myhre et al., 2025), and to inform expectations of its future evolution. Taken together, these pronounced regional differences call for an explicitly process-based, spatially resolved framework.

In this work, we analyze the regional EEI structure to understand the origin of the observed global-mean trend. Previous studies have explored regional decompositions based on latitude bands (Loeb et al., 2024), cloud-top altitude (Loeb et al., 2024), or cloud radiative effect classes (Tselioudis et al., 2025). However, these approaches often mix dynamically distinct regimes and processes, limiting their physical interpretability. To facilitate an attribution of EEI trend to physical drivers, we partition the global domain into distinct dynamical regimes based on physically meaningful quantities, such as vertical velocity and sea level pressure variability. This approach reveals physically consistent regional trends, in line with a broad body of literature on climate forcings and feedbacks. It also supports more informed qualitative expectations of future EEI evolution.

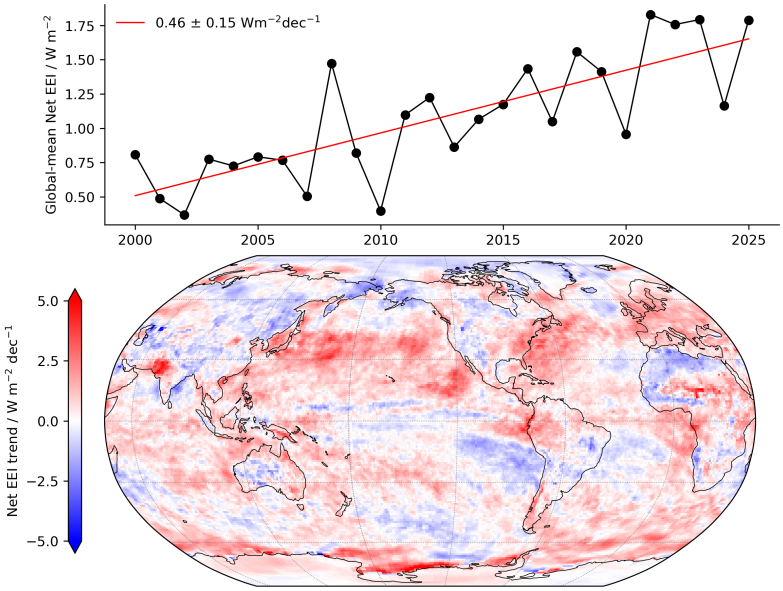

Figure 1. (a) 26 years of annual-mean, global-mean EEI and linear trend from CERES-EBAF Ed4.2.1. (b) Spatial pattern of annual-mean EEI linear trend. Years are defined as starting in March to coincide with the CERES period; we use the full available record for 26 full years from March 2000 – February 2026. Linear trends are computed with OLS regression.

2 Methods

2.1 Data

Our analysis is based on observations of EEI provided by the CERES Energy Balanced and Filled (EBAF) Edition 4.2.1 dataset. CERES comprises a suite of broadband radiometers aboard multiple satellites (Terra, Aqua, and NOAA-20), which measure top-of-atmosphere (TOA) reflected shortwave and emitted longwave radiation, providing a direct observational constraint on the Earth's energy imbalance. These radiance measurements are converted to fluxes using diurnally complete sampling and angular distribution models, and are subsequently combined with auxiliary satellite and reanalysis datasets to produce globally complete, monthly mean radiative fluxes on a 1°×1° grid.

In addition to the all-sky fluxes, EBAF provides clear-sky fluxes, computed with radiative transfer modeling, that can be used to calculate cloud radiative effects, which is particularly useful for this work's targeted, process-based analysis.

To infer the dynamical regimes and the processes driving EEI trends, the ERA-5 reanalysis is used to estimate the atmosphere and surface ocean state. ERA-5 combines past observations with models to estimate atmospheric state at a horizontal resolution of 31 km and 137 vertical levels. For aerosol optical depth (AOD), we use MODIS Aqua and Terra AOD at 550 nm from the Collection 6 (Levy et al., 2013) merged Dark Target-Deep Blue retrieval (Remer et al., 2020).

Our linear trend analysis is based on complete years (2000-2025), defined from March to February. Trends are calculated via a point-wise, ordinary least-squares linear regression on annual or seasonal means. Global- and regional-means are computed using cosine-latitude area-weighting. TOA fluxes from CERES make up a 26-year record, and trends are computed over this period with temporal weighting accounting for the number of days per month, with February weighted to 28.65 days to account for leap years (Oreopoulos et al., 2025; Singer & Pincus, 2026). ERA-5 data are bilinearly interpolated to the CERES $1^\circ \times 1^\circ$ grid.

2.2 Dynamical regime definition

The EEI trend exhibits substantial spatial heterogeneity (Figure 1), suggesting that distinct physical processes contribute differently across regions. To exploit this spatial structure, we partition the globe into a set of dynamical regimes (Figure 2 inset map, and S1) and analyze the contribution of each regime to the global EEI trend.

We define five dynamical regimes using the ERA-5 climatology over 1990–1999. Tropical ascent regions are defined as areas between 40°S and 40°N with climatological mid-tropospheric ascent ($\omega_{500} < 0$). To avoid unrealistically sharp boundaries, the ω_{500} field is smoothed using a Gaussian kernel with a width of 1.5°. Subtropical subsidence regions are defined as areas between 40°S and 40°N with $\omega_{500} > 0$. These regions are further separated into oceanic subsidence regions, associated primarily with stratocumulus cloud decks, and continental subsidence regions, corresponding to desert regions.

Midlatitude storm tracks are identified from sea-level pressure (SLP) variability following Chang et al. (2002). We compute the variance associated with 2–10 day SLP fluctuations and normalize it by the sine of latitude to account for the latitude dependence implied by geostrophic balance, whereby a given pressure anomaly corresponds to stronger winds at lower latitudes (Vallis, 2017). storm track regions are then defined using percentile thresholds of the seasonal SLP variance distribution calculated separately in each hemisphere: the upper 20th percentile in the Northern Hemisphere and the upper 30th percentile in the Southern Hemisphere, since the NH storm activity is concentrated over the Pacific and Atlantic storm tracks (Hoskins & Hodges, 2002), while storm activity over the SH is more uniformly distributed (Hoskins & Hodges, 2005).

Cryosphere regions are defined as areas covered by either perennial land ice or seasonal sea ice. Specifically, these include grid cells with sea ice concentration exceeding 10%, as well as ice-covered land regions including Antarctica, Greenland, and islands north of 75°N (e.g., parts of the Canadian Arctic Archipelago and Svalbard).

Grid cells not assigned to any of the five regimes are grouped into a residual category, which accounts for approximately 1% of the global surface area.

The regime masks are defined statically using the pre-CERES climatology. Consequently, our analysis isolates changes in TOA radiation occurring within fixed geographical regions and does not account for shifts in regime boundaries or changes in regime extent over time. Nevertheless, the inferred contributions of the different regimes to the

global-mean EEI trend are insensitive to the precise baseline period used to construct the masks (not shown).

3 The contribution of dynamical regimes to EEI trends

Figure 2 summarizes the contribution of each regime to the global-mean EEI trend, in the annual-mean and for each individual season. Although there are regions with decreasing EEI evident from the spatial patterns (Figure 1, S1), the regime-average trends are positive for nearly all regimes and seasons. For the global-mean trend, each season contributes significantly, with JJA (0.61±0.24 W m^{-2} dec^{-1}) contributing about twice as much as DJF (0.35 ± 0.31 W m^{-2} dec^{-1}). In the annual-mean, all regimes except NH cryosphere show significant trends at the 95% confidence level; but this is not true at seasonal scale, with DJF showing significant trends for only the tropical ascent and SH cryosphere regime.

Most regimes contribute approximately proportionally given their area — e.g. the oceanic subsidence regime accounts for 27% of global area and contributes 25% of the global-mean EEI trend — except for the cryosphere, where the NH does not contribute, and the SH EEI trend contribution is twice its fractional area. In the annual-mean, the cloud-dominated regimes (storm tracks and oceanic subsidence) contribute 53% of the global-mean trend. Looking at each season separately, no regime can be entirely disregarded.

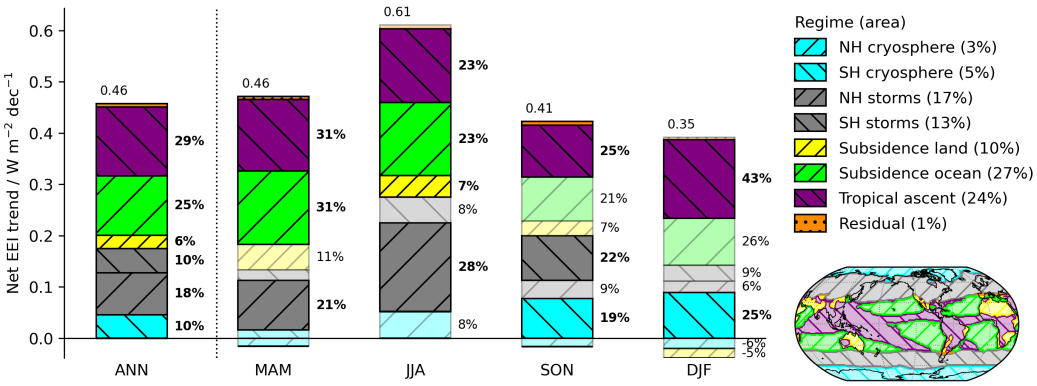

Figure 2. Contribution from each regime to the global-mean EEI trend. Each bar shows a different season, with the annual-mean on the left. The global-mean trend for each season is labeled above each bar. The colors indicate the five regimes, shown in the inset map in the annual-mean. The fractional area of each regime (in the annual-mean) is indicated in the legend. The numbers to the right of each bar indicate the fractional contribution from each regime to the global-mean trend. Bold values and fully opaque colors indicate statistical significance at the 95% confidence level; trend contributions that are not significant are semi-transparent and labeled with non-bold text. Regime contributions below 5% are not labeled.

4 The physical mechanisms behind Earth's heating trends

In Section 4 we discuss each regime one-by-one, identifying physical processes which drive the observed trends. To help identify mechanisms, we consider trends in each component of EEI — clear-sky and cloud radiative effect, shortwave and longwave — as well as different environmental drivers (Figure 3).

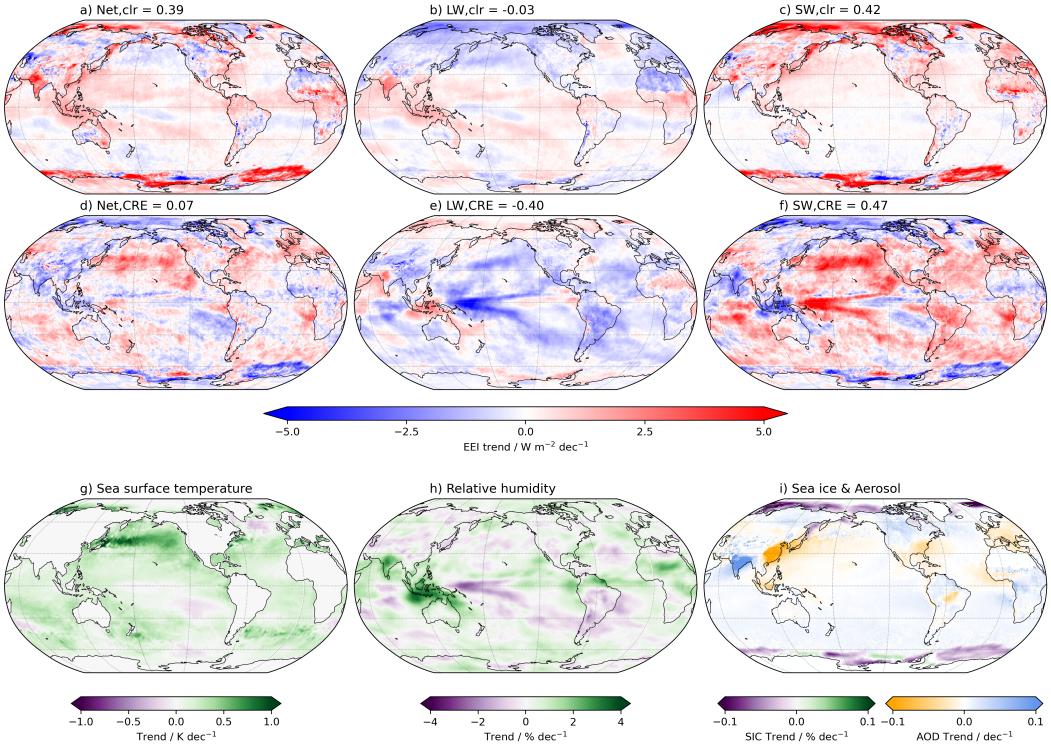

Figure 3. EEI trend decomposition into (a–c) clear-sky and (d–f) cloud radiative effect in the (a,d) net, (b,e) longwave, and (c,f) shortwave in the annual-mean. Also, trends in environmental drivers (g) sea surface temperature, (h) mid-tropospheric relative humidity (600–400 hPa), and (i) sea ice concentration (SIC) and aerosol optical depth (AOD). We show SIC and AOD trends on the same map projection to emphasize that they are both drivers of the SW clear-sky radiation trends.

4.1 Tropical ascent

The tropical ascent (TA) regime covers about 24% of Earth's area and in the annual-mean contributes to 29% of the net EEI global-mean trend. The TA trends are consistent across seasons (0.39–0.66 W m^{-2} dec^{-1}) and statistically significant.

In the TA regime, the largest local EEI trends stem from clouds, but their SW and LW radiative effects virtually cancel each other out (Figure 3d,e,f and 4). This is expected due to the small cloud radiative effect (CRE) of deep convective clouds (Ramanathan et al., 1989; Hartmann et al., 1992; G. Stephens et al., 2018). Therefore, changes in the amount of clouds in the TA regime will result in near zero contribution to EEI trend. The overall positive trend in the TA regime thus results from clear-sky changes – both in the SW and LW (Figure 4).

About half of the TA clear-sky trend is caused by changes in SW radiation. A positive, homogeneous SW clear-sky trend is evident across much of the NH, including the TA regime, and is consistent with anthropogenic aerosol reduction and increased atmospheric water vapor absorption, which both result in heating (Loeb, Johnson, et al., 2021; Loeb, Su, et al., 2021). These trend patterns are mirrored by trends in aerosol optical depth (Figure 3i).

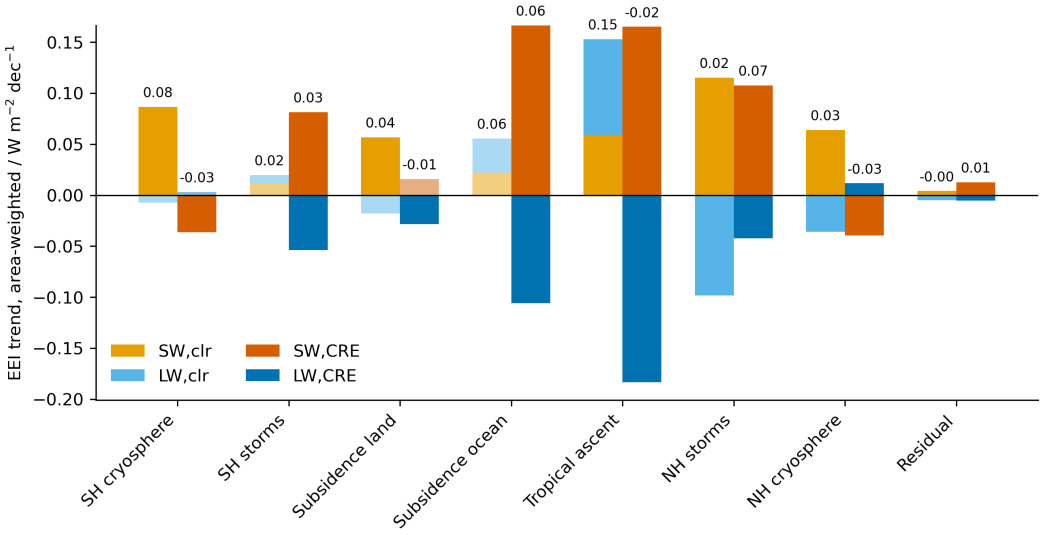

Figure 4. EEI trend contribution from each regime in the annual-mean. The total trend is split into shortwave (oranges) and longwave (blues) and further into clear-sky (left stack) and cloud radiative effect (CRE, right stack). Bar opacity is reduced for trends that are not significant at the 95% confidence level, similar to Figure 2. Total clear-sky and CRE trends are labeled above each stack.

The LW clear-sky component shows a positive EEI trend in the tropical ascent regime (Figure 3b). The pattern suggests a local super-greenhouse effect in the deep tropics, where the increase in greenhouse gases (CO_2 and water vapor) outweighs the Planck response and leads to warming (G. L. Stephens et al., 2016; Koll & Cronin, 2018; Raghuraman et al., 2019; Zhang et al., 2020). To assess the competing contributions of temperature and humidity change, we use a set of analytic equations for idealized spectral radiative transfer from Koll et al. (2023) and Czarnecki and Pincus (2026) to decompose the total clear-sky LW trend (Figure S3). We reconstruct clear-sky LW trends under isolated varying surface temperatures, mid-tropospheric column-integrated relative humidity (RH, Figure 3h), and CO_2 concentration. Using this approach we can reproduce the positive LW clear-sky trend and its dominant patterns (Figure S3, $r = 0.64$).

The increasing CO_2 contributes positively to the clear-sky LW EEI trend, and is offset by the fixed-RH Planck response (Figure S3 c,d). The mid-tropospheric RH changes (Figure 3h) explain a large part of the EEI trend pattern ($r = 0.53$). The RH-driven LW clear-sky EEI trend is generally positive in the deep tropics (Figure S3 b), and reflects regional signals of RH changes like a moistening over the Indian subcontinent, and a dipole in the West Pacific (Figure 3h). Although RH is often assumed to remain constant with warming, this demonstrates that considering RH changes, in addition to warming and CO_2, is necessary to understand the full magnitude and spatial structure of trends in clear-sky LW radiation.

4.2 Subtropical subsidence

4.2.1 Ocean (Stratocumulus)

The subtropical oceanic subsidence regime accounts for 27% of the global area and contributes 25% of the annual-mean EEI trend. The trends are only statistically significant in MAM and JJA.

The oceanic subsidence regime includes the five major stratocumulus (Sc) decks – Californian, Peruvian, Canarian, Namibian, and Australian – where the net EEI trend is driven by SWCRE trends from climatologically endemic low-cloud cover (Figure 3f and 4). The net CRE trend is driven by the SW, though partially compensated by the LW, because Sc clouds have a weak longwave radiative effect due to their warm temperatures and masking by overlying greenhouse gases (Czarnecki & Pincus, 2026).

This SWCRE warming trend is consistent with an observed reduction in low-cloud cover (Goessling et al., 2025; Allan & Merchant, 2025; Ceppi et al., 2026). It is also consistent with a positive low cloud feedback (Sherwood et al., 2020; Myers et al., 2021; Cesana & Del Genio, 2021) and the observed sea surface temperature trends (Figure 3g). These SST trends explain the difference in SW and net CRE trend across the 5 Sc decks but not within the decks, pointing to the importance of the greater SST pattern (Figure S4).

The regions with stronger SST warming have had stronger CRE contributions to EEI increase. In contrast, SST warming has been muted and even slightly cooling in the Peruvian Sc region (Figure 3g), which is consistent with the weak negative EEI trend over this region (Figure 3d). This small negative trend in the Peruvian Sc deck consequently serves to reduce the positive EEI trend from the entire subtropical oceanic subsidence regime.

SST is not the only factor controlling low cloud amount in the Sc regions. However, more complete cloud controlling factor analyses find similar patterns (Ceppi et al. (2026) and their Figure 2 showing decadal trends in SWCRE from low clouds alongside decadal SST trends).

4.2.2 Land (Deserts)

The subtropical subsidence regime over land encompasses the world's major desert regions: Australia, the Sahara/Sahel, some areas over Southern Africa, and the Arabian peninsula. Overall, these desert regions account for about 10% of the global area but only 6% of the contribution to EEI trend. Shortwave clear-sky changes dominate the trend in these regions (Figure 4).

The subtropical land regime shows a positive clear-sky SW trend, about half of which can be attributed to surface albedo reduction. During JJA in particular, we observe a significant positive SW trend over the Sahel region, consistent with a previously documented reduction in surface albedo due to greening (e.g., Chrysoulakis et al., 2019).

4.3 Midlatitudes

The midlatitude storm tracks play an important role in the overall EEI trend, accounting for about 28% of the global-mean annual-mean trend while covering 30% of the global area. The two hemispheres exhibit distinct seasonal signatures: NH trends are dominated by spring and summer (MAMJJA) changes, whereas SH trends peak during spring (SON) (Figure 2, S1). In the SH, the storm track trends are driven almost entirely by cloud-radiative changes, while the NH storm tracks also exhibit substantial clear-sky contributions (Figure 4).

The most prominent midlatitude EEI signal occurs over the North Pacific storm track region, concentrated on its equatorward flank (Figure S1) and driven primarily by changes in SWCRE (Figure 3f). This strong cloud signature is consistent with the central role of extratropical cyclones in organizing midlatitude cloudiness (e.g., Datseris & Stevens, 2021; Hadas et al., 2023). Cyclones exhibit characteristic cloud structures, with deep mid- and high-level clouds and intense precipitation in the warm sector, extensive low-level cloudiness upstream associated with the cold conveyor belt, and enhanced high-

cloud radiative effects in stronger systems (Browning, 1990; Tselioudis & Rossow, 2006; Hadas et al., 2023).

The spatial structure of the EEI trend is consistent with a poleward shift of the storm tracks, which redistributes cloud cover toward higher latitudes where reduced insolation decreases reflected shortwave radiation and enhances net energy uptake (Bender et al., 2012; Tselioudis & Konsta, 2016; Tselioudis et al., 2024). Poleward storm track migration is a robust response to global warming, arising from multiple dynamical mechanisms (Shaw et al., 2016; Tamarin-Brodsky & Kaspi, 2017). In addition, the signal may be amplified during NH summer by a concurrent weakening of storm activity, which has been linked primarily to anthropogenic aerosol forcing (Kang et al., 2024; Chemke & Coumou, 2024).

Although the SWCRE signal is also pronounced in the SH storm tracks, the net EEI trends are less spatially coherent than in the NH and exhibit strong regional and seasonal contrasts (Figure S2 m–p). For example, during spring and summer (SONDJF), negative EEI trends are seen over the South Pacific, in contrast with positive trends over the South Atlantic (Figure S1 a,d). This regional complexity reflects compensation between multiple radiative components. In some seasons, SWCRE changes dominate the signal, whereas in others they are offset by clear-sky or LWCRE contributions, for example during fall (MAM, Figure S2, left column).

In addition to the cloud-driven trends, there are large clear-sky trends in the NH. These are dominated by SW changes, which are linked to anthropogenic aerosol reduction (Loeb, Johnson, et al., 2021; Loeb, Su, et al., 2021) and increased atmospheric water vapor absorption (Loeb, Johnson, et al., 2021; Loeb et al., 2025). The SW clear-sky changes are mirrored in maps of aerosol optical depth trends (Figure 3i). Strong aerosol reductions from China are evident, especially downwind over the Pacific ocean, with reductions also evident from the US east coast and central Europe. Opposite signed aerosol emissions increases are also evident in clear-sky EEI trends over India.

4.4 Polar Cryosphere

The polar cryosphere contributes significantly to the global-mean EEI trend (10%). Moreover, the entire response comes from the SH, which is only 5% of global area (Figure 2). The cryosphere has strongly seasonal behavior, with the NH driving EEI trends in summer (JJA) and the SH driving trends in spring and summer (SONDJF, Figure S2). The importance of the cryosphere regimes comes from the extremely large local EEI trends observed, which are up to four times the global-mean during the summer seasons (1.94 ± 2.07 and 1.86 ± 1.03 W m^{-2} dec^{-1} in NH and SH, respectively).

In both hemispheres, sea ice extent has declined since 2000 (Figure 3i). The Arctic exhibits a relatively steady downward trend throughout this period (e.g., on Climate Change (IPCC), 2023), whereas Antarctic sea ice decline is largely concentrated after 2016 (Purich & Doddridge, 2023). Sea ice melt reduces surface albedo by exposing darker ocean water, thereby enhancing shortwave absorption, resulting in a positive EEI trend, evident particularly in the shortwave clear-sky (Figure 3c). To some extent, cloud masking over sea ice regions results in a compensating negative trend in CRE (Figure 3f).

Despite sea ice declines being larger in the Arctic, the contributions to EEI trends from this albedo reduction are negligible. The hemispheric contrast likely arises from the poleward extent of climatological sea ice. In the NH, albedo changes occur primarily poleward of 70°N, where incoming solar radiation is relatively weaker. In contrast, SH sea ice loss occurs further equatorward (around 60°S), where insolation is higher, thus amplifying the radiative impact of albedo changes. Furthermore, compensation by clouds appears to be stronger in the Arctic, resulting in very little change in net EEI.

5 Looking to the future

By defining dynamical regimes, we are able to more clearly identify physical processes that control the trends in EEI over the 26-year CERES record. Based on these physical insights, we qualitatively assess the future of EEI trends over the coming decades, for which the climate response remains somewhat independent of future emissions scenarios (Booth et al., 2013).

In the tropics, CO_2 increase and water vapor feedback should continue to heat in the clear-sky LW. However, they will be balanced by the Planck response when an equilibrium state is ultimately reached. In the global mean, this timescale (in the absence of continued forcing) is a few decades (Donohoe et al., 2014).

In the subtropical stratocumulus regime, we expect the EEI trend to accelerate in the near future, driven by its SWCRE component. So far, this increase has been partly offset by the brightening of the Peruvian stratocumulus deck in response to locally cooling SSTs. Importantly, however, recent findings indicate that east Pacific SST cooling has slowed relative to the pre-CERES period (Figure 3g), consistent with CMIP5/6 projections that this region will warm over the long term (Wills et al., 2022).

Over the midlatitudes, the positive trends associated with the poleward shift of the storm tracks are expected to persist, as storm tracks are projected to continue shifting poleward at least through the end of the century (Shaw et al., 2016; Tamarin-Brodsky & Kaspi, 2017). However, the mixed SH response across seasons (Figure S2 m–p) indicates that other physical processes play a role in shaping the overall response, which adds ambiguity to the future trend.

The evolution of the strong positive trends over the Southern Ocean cryosphere is likely to be seasonally dependent. During spring (SON), the trend linked to earlier melt onset is expected to continue, as warming advances the timing of the melt season (Himmich et al., 2024). The larger summer (DJF) trend is less likely to accelerate, since summer sea ice is limited in area (Docquier et al., 2025).

More generally, while many of the observed EEI trends are likely to persist over the coming decades, not all changes during the CERES period necessarily reflect a long-term forced response. The interannual variability associated with the El Niño Southern Oscillation (ENSO) is evident in the low-latitude regimes, and the strength of the trends fluctuates with the number of strong ENSO events included in the record (Loeb et al., 2024; Hakuba et al., 2024). Additionally, the regional signals linked to aerosol trends may differ in the future as regional emissions change. Unlike greenhouse-gas forcing, aerosol forcing evolves non-linearly and non-monotonically in response to changing emissions and air-quality regulations (Quaas et al., 2022; Shi et al., 2022; Wang & Wen, 2022). Consequently, some regional EEI trends may weaken, reverse, or evolve differently in the future than would be expected from greenhouse-gas-driven warming alone.

6 Conclusion

The recent increase in Earth's energy imbalance is not spatially uniform, reflecting the combined influence of distinct physical mechanisms operating across different dynamical regimes. By partitioning the globe into these dynamical regimes based on climatological circulation metrics, we show that much of the observed EEI trend can be understood in terms of physically coherent responses that align with existing understanding of climate forcings and feedbacks. By comparing the fractional area of each regime to its fractional contribution to global-mean EEI trend, we note that most regimes have relatively proportional contributions, although the SH cryosphere stands out with a larger-than-average EEI increase.

The tropical ascent regime contributes the largest fraction to the global EEI increase, primarily through longwave clear-sky changes, associated with the greenhouse effect from increased CO_2 and water vapor. In the subtropical oceanic subsidence regime, trends are dominated by shortwave cloud radiative effects linked to reductions in stratocumulus cloud cover, consistent with positive low-cloud feedbacks and regional SST trends. Midlatitude storm track regimes exhibit strong cloud-driven trends consistent with poleward storm track shifts, together with important aerosol-driven shortwave clear-sky changes in the Northern Hemisphere. Meanwhile, the strongest local EEI trends occur in the polar cryosphere, where sea ice loss enhances shortwave absorption, with particularly strong contributions from the Southern Hemisphere. In total, cloud-dominated regimes (stratocumulus and storm tracks) account for more than half of the global-mean EEI trend, but no single regime or season can individually explain the observations.

Earth's growing energy imbalance presents a challenge to understanding both because of the fast rate of increase and because most climate models fail to capture the recent observed EEI trends. In this paper we demonstrate that a dynamical regime decomposition provides a pathway for mechanistic interpretation of recent EEI increase by linking observed radiation trends to the underlying physical processes governing Earth's climate response. Looking forward, a similar approach may offer a powerful pathway for addressing model–observation discrepancies. By identifying consistent dynamical regimes across observations and models, within-regime responses can be compared separately from the frequency of occurrence of regimes. At the same time, isolating the dominant physical processes operating within each regime enables a process-based evaluation of climate models and a pathway for constraining the future evolution of Earth's energy imbalance.

Open Research Section

CERES-EBAF data is available online: `https://ceres-tool.larc.nasa.gov`. Scripts to reproduce all analyses are available here (and will be archived on Zenodo upon acceptance): `https://github.com/OrHadasAtmosphere/EEI_trends/`.

Conflict of Interest declaration

The authors declare there are no conflicts of interest for this manuscript.

Acknowledgments

This paper was conceived during a workshop financially supported, organized, and hosted by the Max Planck Society at Schloss Ringberg in March 2026. The authors are grateful for inspiring discussions with the workshop participants.

References

Allan, R. P., & Merchant, C. J. (2025). Reconciling Earth's growing energy imbalance with ocean warming. *Environmental Research Letters*, *20*(4), 044002. doi: 10.1088/1748-9326/adb448

Bender, F. A.-M., Ramanathan, V., & Tselioudis, G. (2012). Changes in extratropical storm track cloudiness 1983–2008: Observational support for a poleward shift. *Climate Dynamics*, *38*(9–10), 2037–2053. doi: 10.1007/s00382-011-1065-6

Booth, B. B. B., Bernie, D., McNeall, D., Hawkins, E., Caesar, J., Boulton, C., ... Sexton, D. M. H. (2013). Scenario and modelling uncertainty in global mean temperature change derived from emission-driven global climate models. *Earth System Dynamics*, *4*(1), 95–108. Retrieved from `https://esd.copernicus.org/articles/4/95/2013/` doi: 10.5194/esd-4-95-2013

Browning, K. A. (1990). Organization of clouds and precipitation in extratropical cyclones. In *Extratropical cyclones: the erik palmén memorial volume* (pp. 129–153). Springer.

Ceppi, P., Wilson Kemsley, S., Andersen, H., Andrews, T., Kramer, R. J., Nowack, P., ... Zelinka, M. D. (2026). Emerging low-cloud feedback and adjustment in global satellite observations. *Atmospheric Chemistry and Physics*, *26*(6), 4153–4171. doi: 10.5194/acp-26-4153-2026

Cesana, G. V., & Del Genio, A. D. (2021). Observational constraint on cloud feedbacks suggests moderate climate sensitivity. *Nature Climate Change*. doi: 10.1038/s41558-020-00970-y

Chang, E. K., Lee, S., & Swanson, K. L. (2002). Storm track dynamics. *Journal of climate*, *15*(16), 2163–2183.

Chemke, R., & Coumou, D. (2024). Human influence on the recent weakening of storm tracks in boreal summer. *npj Climate and Atmospheric Science*, *7*(1), 86.

Chrysoulakis, N., Mitraka, Z., & Gorelick, N. (2019). Exploiting satellite observations for global surface albedo trends monitoring. *Theoretical and Applied Climatology*, *137*(1), 1171–1179. doi: 10.1007/s00704-018-2663-6

Czarnecki, P., & Pincus, R. (2026). How clear-sky spectral overlap shapes radiation in cloudy atmospheres. *ESS Open Archive*, *2026*(0309). doi: 10.22541/essoar.176031268.82054152/v2

Datseris, G., & Stevens, B. (2021). Earth's albedo and its symmetry. *AGU Advances*, *2*(3), e2021AV000440.

Docquier, D., Massonnet, F., Richaud, B., Fichefet, T., Goosse, H., Mezzina, B., ... Vannitsem, S. (2025). Drivers of summer antarctic sea-ice extent at interannual time scale in cmip6 large ensembles based on information flow. *Climate Dynamics*, *63*(10), 374.

Donohoe, A., Armour, K. C., Pendergrass, A. G., & Battisti, D. S. (2014). Shortwave and longwave radiative contributions to global warming under increasing co2. *Proceedings of the National Academy of Sciences*, *111*(47), 16700-16705. doi: 10.1073/pnas.1412190111

Goessling, H. F., Rackow, T., & Jung, T. (2025). Recent global temperature surge intensified by record-low planetary albedo. *Science*, *387*(6729), 68–73. doi: 10.1126/science.adq7280

Hadas, O., Datseris, G., Blanco, J., Bony, S., Caballero, R., Stevens, B., & Kaspi, Y. (2023). The role of baroclinic activity in controlling earth's albedo in the present and future climates. *Proceedings of the National Academy of Sciences*, *120*(5), e2208778120.

Hakuba, M. Z., Fourest, S., Boyer, T., Meyssignac, B., Carton, J. A., Forget, G., ... Von Schuckmann, K. (2024). Trends and Variability in Earth's Energy Imbalance and Ocean Heat Uptake Since 2005. *Surveys in Geophysics*, *45*(6), 1721–1756. doi: 10.1007/s10712-024-09849-5

Hartmann, D. L., Ockert-Bell, M. E., & Michelsen, M. L. (1992). The effect of cloud type on earth's energy balance: Global analysis. *Journal of Climate*, *5*(11), 1281 - 1304. doi: 10.1175/1520-0442(1992)005⟨1281:TEOCTO⟩2.0.CO;2

Held, I. M., Winton, M., Takahashi, K., Delworth, T., Zeng, F., & Vallis, G. K. (2010). Probing the fast and slow components of global warming by returning abruptly to preindustrial forcing. *Journal of Climate*, *23*(9), 2418 - 2427. doi: 10.1175/2009JCLI3466.1

Himmich, K., Vancoppenolle, M., Stammerjohn, S., Bocquet, M., Madec, G., Sallée, J.-B., & Fleury, S. (2024). Thermodynamics drive post-2016 changes in the antarctic sea ice seasonal cycle. *Journal of Geophysical Research: Oceans*, *129*(8), e2024JC021112.

Hodnebrog, O., Myhre, G., Jouan, C., Andrews, T., Forster, P. M., Jia, H., ... Schulz, M. (2024). Recent reductions in aerosol emissions have increased

Earth's energy imbalance. *Communications Earth & Environment*, *5*(1), 166. doi: 10.1038/s43247-024-01324-8

Hoskins, B. J., & Hodges, K. I. (2002). New perspectives on the northern hemisphere winter storm tracks. *Journal of the Atmospheric Sciences*, *59*(6), 1041–1061.

Hoskins, B. J., & Hodges, K. I. (2005). A new perspective on southern hemisphere storm tracks. *Journal of climate*, *18*(20), 4108–4129.

Kang, J. M., Shaw, T. A., & Sun, L. (2024). Anthropogenic aerosols have significantly weakened the regional summertime circulation in the northern hemisphere during the satellite era. *Agu Advances*, *5*(6), e2024AV001318.

Koll, D. D. B., & Cronin, T. W. (2018). Earth's outgoing longwave radiation linear due to H_2 O greenhouse effect. *Proceedings of the National Academy of Sciences*, *115*(41), 10293–10298. doi: 10.1073/pnas.1809868115

Koll, D. D. B., Jeevanjee, N., & Lutsko, N. J. (2023, August). An Analytic Model for the Clear-Sky Longwave Feedback. *Journal of the Atmospheric Sciences*, *80*(8), 1923–1951. doi: 10.1175/JAS-D-22-0178.1

Levy, R. C., Mattoo, S., Munchak, L. A., Remer, L. A., Sayer, A. M., Patadia, F., & Hsu, N. C. (2013). The Collection 6 MODIS aerosol products over land and ocean. *Atmospheric Measurement Techniques*, *6*(11), 2989–3034. doi: 10.5194/amt-6-2989-2013

Loeb, N. G., Ham, S.-H., Allan, R. P., Thorsen, T. J., Meyssignac, B., Kato, S., ... Lyman, J. M. (2024). Observational Assessment of Changes in Earth's Energy Imbalance Since 2000. *Surveys in Geophysics*. doi: 10.1007/s10712-024-09838-8

Loeb, N. G., Johnson, G. C., Thorsen, T. J., Lyman, J. M., Rose, F. G., & Kato, S. (2021). Satellite and Ocean Data Reveal Marked Increase in Earth's Heating Rate. *Geophysical Research Letters*, *48*(13), e2021GL093047. doi: 10.1029/2021GL093047

Loeb, N. G., Su, W., Bellouin, N., & Ming, Y. (2021). Changes in clear-sky shortwave aerosol direct radiative effects since 2002. *Journal of Geophysical Research: Atmospheres*, *126*(5), e2020JD034090. (e2020JD034090 2020JD034090) doi: https://doi.org/10.1029/2020JD034090

Loeb, N. G., Thorsen, T. J., Kato, S., Rose, F. G., Hodnebrog, O., & Myhre, G. (2025). Emerging hemispheric asymmetry of Earth's radiation. *Proceedings of the National Academy of Sciences*, *122*(40), e2511595122. doi: 10.1073/pnas.2511595122

Mauritsen, T., Tsushima, Y., Meyssignac, B., Loeb, N. G., Hakuba, M., Pilewskie, P., ... Zelinka, M. D. (2025). Earth's Energy Imbalance More Than Doubled in Recent Decades. *AGU Advances*, *6*(3), e2024AV001636. doi: 10.1029/2024AV001636

Minière, A., Von Schuckmann, K., Sallée, J.-B., & Vogt, L. (2023). Robust acceleration of Earth system heating observed over the past six decades. *Scientific Reports*, *13*(1), 22975. doi: 10.1038/s41598-023-49353-1

Myers, T. A., Scott, R. C., Zelinka, M. D., Klein, S. A., Norris, J. R., & Caldwell, P. M. (2021). Observational constraints on low cloud feedback reduce uncertainty of climate sensitivity. *Nature Climate Change*(January 1982). doi: 10.1038/s41558-021-01039-0

Myhre, G., Hodnebrog, O., Loeb, N., & Forster, P. M. (2025). Observed trend in Earth energy imbalance may provide a constraint for low climate sensitivity models. *Science*, *388*(6752), 1210–1213. doi: 10.1126/science.adt0647

on Climate Change (IPCC), I. P. (2023). Ocean, cryosphere and sea level change. In *Climate change 2021 – the physical science basis: Working group i contribution to the sixth assessment report of the intergovernmental panel on climate change* (p. 1211–1362). Cambridge University Press.

Oreopoulos, L., Cho, N., & Lee, D. (2025). The role of Earth's major cloud systems

in the hemispheric albedo symmetry. *Journal of Climate*. doi: 10.1175/JCLI-D-25-0242.1

Park, C., & Soden, B. J. (2025). Negligible contribution from aerosols to recent trends in Earth's energy imbalance. *Science Advances*, *11*(48), eadv9429. doi: 10.1126/sciadv.adv9429

Purich, A., & Doddridge, E. W. (2023). Record low antarctic sea ice coverage indicates a new sea ice state. *Communications Earth & Environment*, *4*(1), 314.

Quaas, J., Jia, H., Smith, C., Albright, A. L., Aas, W., Bellouin, N., ... Schulz, M. (2022). Robust evidence for reversal of the trend in aerosol effective climate forcing. *Atmospheric Chemistry and Physics*, *22*(18), 12221–12239. doi: 10.5194/acp-22-12221-2022

Raghuraman, S. P., Paynter, D., & Ramaswamy, V. (2019). Quantifying the drivers of the clear sky greenhouse effect, 2000–2016. *Journal of Geophysical Research: Atmospheres*, *124*(21), 11354-11371. doi: https://doi.org/10.1029/2019JD031017

Raghuraman, S. P., Paynter, D., & Ramaswamy, V. (2021). Anthropogenic forcing and response yield observed positive trend in Earth's energy imbalance. *Nature Communications*, *12*(1), 4577. doi: 10.1038/s41467-021-24544-4

Ramanathan, V., Cess, R. D., Harrison, E. F., Minnis, P., Barkstrom, B. R., Ahmad, E., & Hartmann, D. (1989). Cloud-radiative forcing and climate: Results from the earth radiation budget experiment. *Science*, *243*(4887), 57-63. doi: 10.1126/science.243.4887.57

Remer, L. A., Levy, R. C., Mattoo, S., Tanré, D., Gupta, P., Shi, Y., ... Holben, B. N. (2020). The Dark Target Algorithm for Observing the Global Aerosol System: Past, Present, and Future. *Remote Sensing*, *12*(18), 2900. doi: 10.3390/rs12182900

Shaw, T., Baldwin, M., Barnes, E. A., Caballero, R., Garfinkel, C., Hwang, Y.-T., ... others (2016). Storm track processes and the opposing influences of climate change. *Nature Geoscience*, *9*(9), 656–664.

Sherwood, S. C., Webb, M. J., Annan, J. D., Armour, K. C., Forster, P. M., Hargreaves, J. C., ... Zelinka, M. D. (2020). An Assessment of Earth's Climate Sensitivity Using Multiple Lines of Evidence. *Reviews of Geophysics*, *58*(4), e2019RG000678. doi: 10.1029/2019RG000678

Shi, J.-R., Kwon, Y.-O., & Wijffels, S. E. (2022). Two Distinct Modes of Climate Responses to the Anthropogenic Aerosol Forcing Changes. *Journal of Climate*, *35*(11), 3445–3457. doi: 10.1175/JCLI-D-21-0656.1

Singer, C. E., & Pincus, R. (2026). Southern Ocean Clear-Sky Brightening From Sea Spray Aerosol Increase Drives Departure From Hemispheric Albedo Symmetry. *Geophysical Research Letters*, *53*(1), e2025GL119637. doi: 10.1029/2025GL119637

Stephens, G., Winker, D., Pelon, J., Trepte, C., Vane, D., Yuhas, C., ... Lebsock, M. (2018). Cloudsat and calipso within the a-train: Ten years of actively observing the earth system. *Bulletin of the American Meteorological Society*, *99*(3), 569 - 581. doi: 10.1175/BAMS-D-16-0324.1

Stephens, G. L., Kahn, B. H., & Richardson, M. (2016). The super greenhouse effect in a changing climate. *Journal of Climate*, *29*(15), 5469 - 5482. doi: 10.1175/JCLI-D-15-0234.1

Tamarin-Brodsky, T., & Kaspi, Y. (2017). Enhanced poleward propagation of storms under climate change. *Nature geoscience*, *10*(12), 908–913.

Tselioudis, G., & Konsta, D. (2016). The 'storm curtain' effect: Poleward shift of clouds, their radiative effects, and the role of midlatitude storms. In *Perspectives on atmospheric sciences* (pp. 725–731). Springer.

Tselioudis, G., Remillard, J., Jakob, C., & Rossow, W. B. (2025). Contraction of the World's Storm-Cloud Zones the Primary Contributor to the 21st Century Increase in the Earth's Sunlight Absorption. *Geophysical Research Letters*,

52(11), e2025GL114882. doi: 10.1029/2025GL114882

Tselioudis, G., & Rossow, W. B. (2006). Climate feedback implied by observed radiation and precipitation changes with midlatitude storm strength and frequency. *Geophysical research letters*, *33*(2).

Tselioudis, G., Rossow, W. B., Bender, F., Oreopoulos, L., & Remillard, J. (2024). Oceanic cloud trends during the satellite era and their radiative signatures. *Climate Dynamics*, *62*(9), 9319–9332. doi: 10.1007/s00382-024-07396-8

Vallis, G. K. (2017). *Atmospheric and oceanic fluid dynamics*. Cambridge University Press.

Von Schuckmann, K., Minière, A., Gues, F., Cuesta-Valero, F. J., Kirchengast, G., Adusumilli, S., ... Zemp, M. (2023). Heat stored in the Earth system 1960–2020: Where does the energy go? *Earth System Science Data*, *15*(4), 1675–1709. doi: 10.5194/essd-15-1675-2023

Wang, H., & Wen, Y.-J. (2022). Climate response to the spatial and temporal evolutions of anthropogenic aerosol forcing. *Climate Dynamics*, *59*(5-6), 1579–1595. doi: 10.1007/s00382-021-06059-2

Wills, R. C. J., Dong, Y., Proistosecu, C., Armour, K. C., & Battisti, D. S. (2022). Systematic climate model biases in the large-scale patterns of recent sea-surface temperature and sea-level pressure change. *Geophysical Research Letters*, *49*(17), e2022GL100011. doi: https://doi.org/10.1029/2022GL100011

Winton, M., Takahashi, K., & Held, I. M. (2010). Importance of ocean heat uptake efficacy to transient climate change. *Journal of Climate*, *23*(9), 2333 - 2344. doi: 10.1175/2009JCLI3139.1

Zhang, Y., Jeevanjee, N., & Fueglistaler, S. (2020). Linearity of outgoing longwave radiation: From an atmospheric column to global climate models. *Geophysical Research Letters*, *47*(17), e2020GL089235. (e2020GL089235 10.1029/2020GL089235) doi: https://doi.org/10.1029/2020GL089235